Supporting Information

Favorably Adjusting the Pore Characteristics of Copper Sulfide by Template Regulation for Vapor-Phase Elemental Mercury Immobilization

Wei Zheng[a], Zequn Yang[a], Jianping Yang[a], Wenqi Qu[a], Yong Feng[b], Shaojian Jiang[a], Shilin Zhao[a], Kaimin Shih[c], Hailong Li[a**]*

a. School of Energy Science and Engineering, Central South University, Changsha, 410083, China

b. Environmental Research Institute, South China Normal University, Guangzhou, 510631, China

c. Department of Civil Engineering, The University of Hong Kong, Hong Kong SAR, China

Revision Submitted to

Journal of Materials Chemistry A

To whom correspondence should be addressed:

*TEL: +86-15675117541

E-mail: Zequn_Yang@hotmail.com

**TEL: +86-18670016725

E-mail: hailongli18@gmail.com

Kinetic Simulation

The pseudo-first order kinetic model was used to predict the Hg^0 adsorption capacity based on an ~80% breakthrough dataset. The Hg^0 adsorption rate was proportional to the difference between the equilibrium capacity and the adsorbed amount at any time, as described as follows:

$$\frac{\mathrm{d}Q_t}{dt} = k_1(Q_e - Q_t) \tag{S1}$$

Equation (3) could be modified to the following equation based on the initial conditions of t=0, Q_t=0:

$$Q_t = Q_e(1 - e^{-k_1 t}) \tag{S2}$$

where the pseudo-first-order kinetic constant (k_1, min^{-1}) can be determined by fitting the adsorption breakthrough curve.

Besides, the pseudo-second-order kinetic model was also adopted to simulate the Hg^0 adsorption behavior, which could be described by equation (S3):

$$\frac{dQ_t}{dt} = k_2(Q_e - Q_t)^2 \tag{S3}$$

Equation (S3) could be modified to the following equation based on the initial conditions of t=0, Q_t=0:

$$\frac{t}{Q_t} = \frac{1}{k_2 Q_e^2} + \frac{1}{Q_e}t \tag{S4}$$

where the pseudo-second-order kinetic constant (k_2, mg g^{-1} min^{-1}) can be determined by fitting the adsorption breakthrough curve.

Hg-TPD Test

First, the fresh sorbent was pretreated at its optimal reaction temperature (75 ^{o}C) under ~100 μg m^{-3} carried by N_2 for a continuous 30 min. Subsequently, the inlet Hg^0 was cut off, and the Hg-laden sorbent was purged by pure N_2 at a same temperature until the outlet Hg^0 equaling to zero. Then, the temperature stepwise increased from 75 to 350 ^{o}C with the heating rate of 10 ^{o}C min^{-1}. During this process, the desorbed/decomposed mercury was continuously recorded by the on-line mercury analyzer (VM3000, Mercury Instrument, Inc.).

List of Tables:

Table S1. Experimental conditions

Experiments	Materials	Carrier gas (1L min^{-1})	Temperature (℃)
Set I	Cu-BTC CuS-BTCs Nano-CuS	Pure N_2	75
Set II	9CuS-BTC	Pure N_2	25-100
Set III	9CuS-BTC	Pure N_2	75
Set IV	9CuS-BTC	Pure N_2 N_2 + 5% O_2 N_2 +5% O_2 + 100 ppm SO_2 SFG	75

SFG: Simulated flue gas (5% O_2, 100 ppm SO_2 and 8% H_2O carried by N_2)

Table S2. Performance comparison among benchmark metal sulfides

Sorbents	Carrier gas	Inlet Hg^0 concentration ($\mu g\ m^{-3}$)	Optimal temperature (°C)	Hg^0 adsorption capacities ($mg\ g^{-1}$)	Hg^0 adsorption rates ($\mu g\ g^{-1}\ min^{-1}$)	Reference
CuS-BTC	N_2	100	75	208.50	97.30	This work
$FeWS_x/TiO_2$	N_2	4300	100	9.00	25.00	[S1]
$[MoS_4]^{2-}$/CoFe-LDH	N_2 + 4% O_2	350	75	16.39	5.00	[S1]
Disordered MoS_2	N_2 + 6% O_2 + 6% SO_2	240	100	16.39	3.83	[S2]
Mn-SnS_2	N_2 + 5% O_2	300	150	0.57	9.45	[S1]
Fe-ZnS	Air	1600	20	8.65	4.82	[S1]
MoS_3/γ-Fe_2O_3	N_2	110	60	12.80	1.55	[S1]
Co_9S_8-PC	N_2	210	100	43.18	12.15	[S3]
MoS_3/TiO_2	N_2	280	60	28.10	24.80	[S1]
$Co_xZn_{1-x}S$	N_2 + O_2	1100	50	46.01	17.00	[S1]
ZnO@CuS	N_2	800	75	60.53	16.81	[S4]
Fe_3O_4@CuS	N_2	90	75	88.70	13.25	[S1]
nano-CuS	N_2	90	75	122.40	13.56	[S1]
Sulfurated Fe-Ti spinel	N_2	4300	60	48.60	43.30	[S1]
$FeMoS_x/TiO_2$	N_2	4300	60	41.80	72.20	[S1]
Co_3S_4	N_2	1300	100	43.03	84.10	[S1]
Sulfureted MoO_3/Fe-Ti spinel	SFG	4300	60	66.30	93.30	[S1]

Simulated flue gas (SFG) contains N_2, O_2, SO_2, and H_2O.

List of Figures:

Figure S1. XRD patterns of different samples

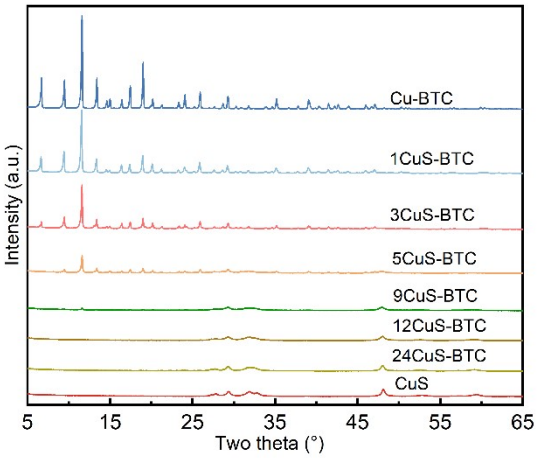

Figure S2. Areas as selected to conduct the EDS characterizations of Cu-BTC, 9CuS-BTC and 24CuS-BTC

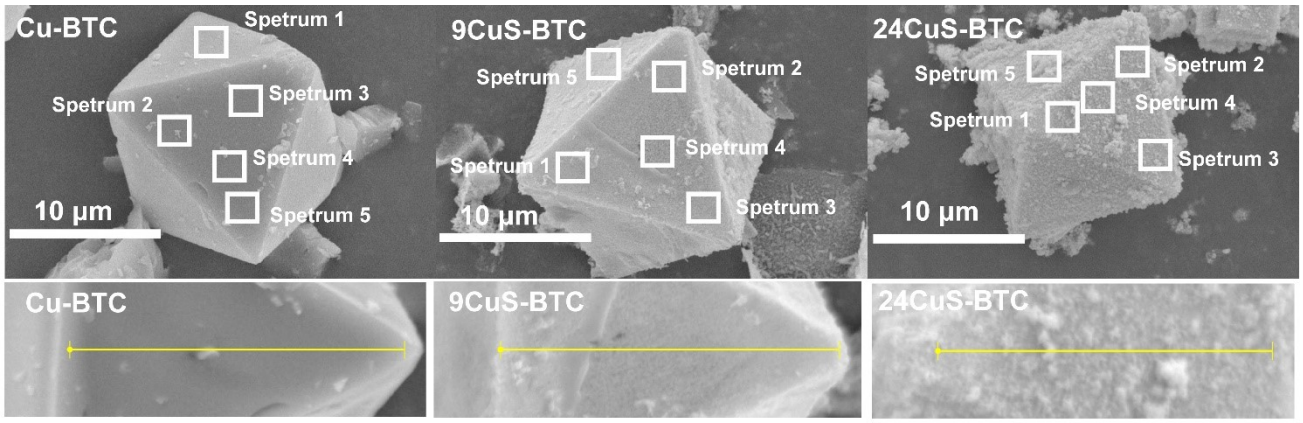

Figure S3. EDS line scanning of Cu-BTC, 9CuS-BTC, and 24CuS-BTC

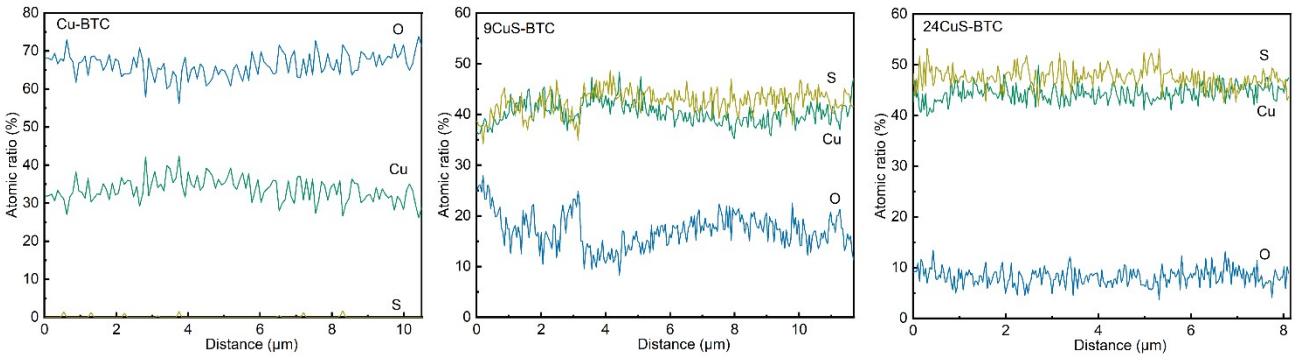

Figure S4. EDS mappings of Cu-BTC, 9CuS-BTC, and 24CuS-BTC

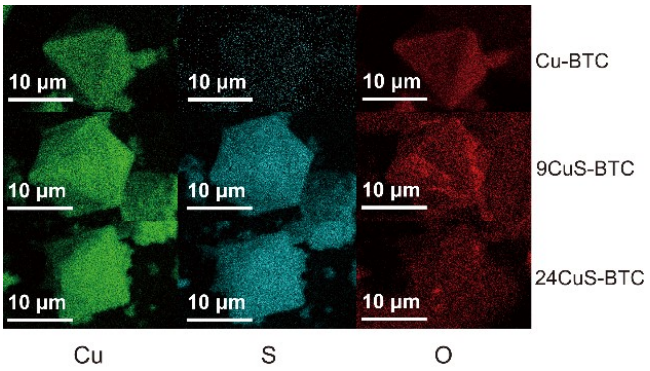

Figure S5. The distribution of micropores in Cu-BTC

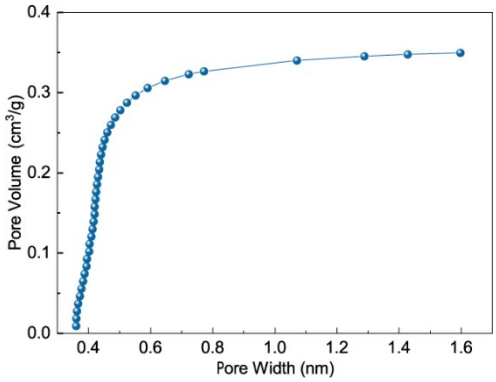

Figure S6. A diagrammatical illustration on the transformation of Cu-BTC to 24CuS-BTC

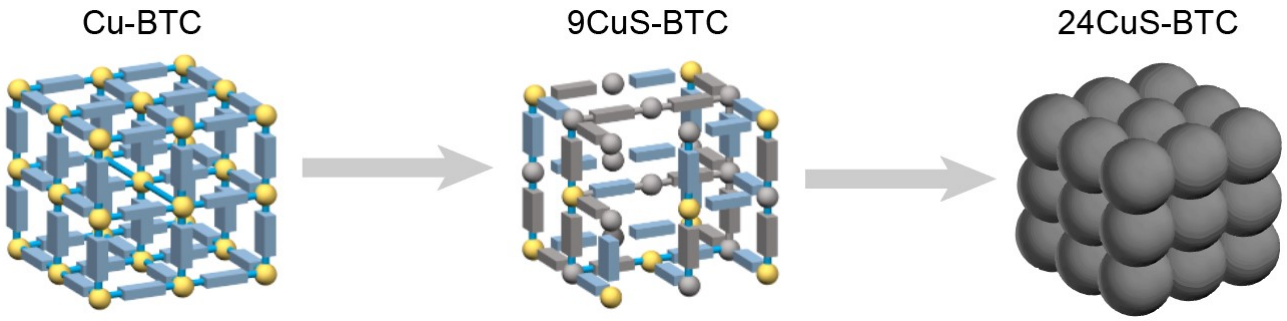

Figure S7. Comparison between the high-resolution SEM images of 9CuS-BTC and 24CuS-BTC

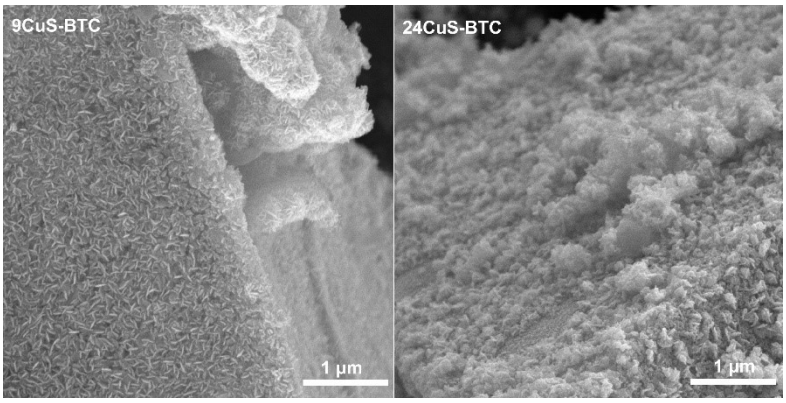

Figure S8. The breakthrough curve of 9CuS-BTC

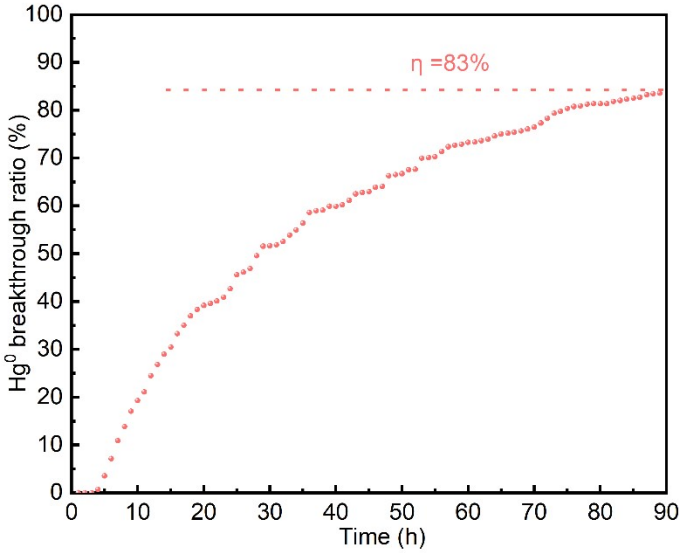

Reference

[1] W. Zheng, H. Li, Z. Yang, J. Yang, W. Qu, F. Meng, Y. Feng, Z. Xu, X. Guo, *Chem. Eng. J.*, 2021, **411**, 128608.

[2] H. Liu, C. Liu, K. Xiang, C. Li, X. Xie, H. Chen, P. Wang, F. Shen, *ACS ES&T Eng.*, 2021, **1**, 1258-1266.

[3] S. Yang, C. Liu, P. Wang, H. Yi, F. Shen, H. Liu, *J. Hazard. Mater*., 2021, **412**, 124970.

[4] Q. Hong, H. Xu, J. Li, W. Huang, P. Liu, Z. Qu and N. Yan, *Chem. Eng. J.*, 2021, **420**, 127592.